

Improvement in Determination of Ice Water Content from Two-Dimensional Particle Imagery. Part II: Applications to Collected Data

R. PAUL LAWSON AND BRAD A. BAKER

SPEC, Inc., Boulder, Colorado

(Manuscript received 29 December 2004, in final form 23 January 2006)

ABSTRACT

In Part I of this two-part series, a new relationship for ice particle mass M was derived based on an expanded dataset of photographed ice particles and melted drops. The new relationship resulted in a reduction of nearly 50% in the rms error in M . In this paper, new relationships for computing particle mass and ice water content from 2D particle imagery are compared with other relationships previously used in the literature. Comparison of the old and new relationships, when applied to data collected in natural clouds, shows that results using the old relationships differ from the new relationships by up to a factor of 3, depending on particle size and shape. One of the new relationships can be applied to existing (archived) datasets of two-dimensional images, provided that the number of occulted pixels in each image (i.e., projected area) is available.

1. Introduction

Baker and Lawson (2006a, hereinafter Part I), introduce a new relationship for calculating the mass M of ice particles from two-dimensional particle images. The relationship was developed via a reanalysis of an expanded dataset¹ of photographed ice particle images and equivalent melted drops previously collected and analyzed by Mitchell et al. (1990, hereinafter M90). Mason (1957) originally derived a power-law relationship to compute M from maximum particle dimension L . Several investigators have since developed relationships between M and L based on photographs of ice particles and melted drop diameters (e.g., Davis 1974; Locatelli and Hobbs 1974; M90 and Brown and Francis

1995, hereinafter BF95). These relationships take the form

$$M = \alpha X^\beta, \quad (1)$$

where M is particle mass, $X = L$, and α and β are constants determined from linear regression on a population of particle image and mass pairs. The Part I relationship substitutes a combined single parameter (CSP) for X in (1),

$$X = \text{CSP} = AW(2L + 2W)/P, \quad (2)$$

where L is the particle maximum dimension, W is width, defined as the maximum dimension transverse to L , A is projected area, and P is perimeter of the ice particle image. Part I explains the reasoning behind the formulation of (2), which is an attempt to estimate an intrinsically three-dimensional quantity, particle mass, from properties of a two-dimensional image.

Part I shows that, when applied to an expanded M90 dataset using $X = \text{CSP}$, (1) results in a reduction of nearly 50% in the RMS error in M , when compared with using $X = L$ in (1). Part I also found that a nearly 50% improvement is also obtained using $X = A$ alone. The improvement that Part I found in predicted mass using $X = \text{CSP}$ or A can be explained logically, because both CSP and A contain information on two-dimensional particle shape, whereas L contains information on only one dimension. For the sake of brevity, the

¹ M90 processed 831 of the images on the fifty-one 35-mm photographic slides. Of these 831, 630 were segregated into 17 habit (shape) categories and used in their study. For this study 549 of the 831 ice particles and equivalent melted drop images that we could unambiguously identify and process with CPIview were selected for reanalysis. An additional 315 images that had not been processed by M90 were processed by SPEC personnel, bringing the total number of images processed in this study to 864.

Corresponding author address: R. Paul Lawson, SPEC, Inc., 3022 Sterling Circle, Suite 200, Boulder, CO 80301.
E-mail: paulson@specinc.com

relationship using $X = A$ in (1) will be referred to as Part I_{Area} , and using $X = \text{CSP}$ in (1) will be referred to as Part I_{CSP} . Using Part I_{CSP} or Part I_{Area} has the added advantage that it is not necessary to separate the ice particle images into separate habit categories, which is often intractable using conventional particle imagery, such as the 2D cloud (2D-C) and the precipitation (2D-P) particle imaging probes described by Knollenberg (1970, 1981).

Heymsfield et al. (2002, hereinafter H02) also included A together with L and were able to improve IWC estimates from 2D image data for certain crystal types. They established power-law relationship for columnar, planar, spatial rosette, side plane, and aggregate type ice crystals via a complex combination of theoretical derivations based on simple ideal shapes, the numerical modeling of more complex shapes, and the incorporation of fits from various sets of observational data. However, the H02 relationships require that the ice crystal dataset first be segregated into the various crystal types, and, as explained above, this cannot be accomplished confidently on a particle-by-particle basis using 2D imagery. Part I applied the H02 method to the expanded M90 dataset of ice crystal images to determine how well it would perform on a dataset with measured particle masses. A statistical analysis showed that the RMS error using H02 was 5 times that of the RMS error using Part I_{CSP} or Part I_{Area} .

Furthermore, Part I found that sorting particles from the expanded M90 dataset into 17 habit categories and applying (1) with different values of α and β for each category did not improve the prediction of mass as much as using Part I_{CSP} or Part I_{Area} . This is because, as shown by Part I, CSP and even A alone account for particle shape better than habit segregation with L alone as the predictor. Also, the expanded M90 dataset is not extensive enough to derive meaningful separate relationships for each habit class represented. Thus, Part I found that evaluation of particle shape is a very important factor in improving the accuracy of determining M from 2D imagery, and based on the expanded M90 dataset, using CSP or A resulted in the best performance of the methods tested in accounting for particle shape.

The Part I relationships can be applied to archived datasets of 2D particle images, possibly improving the accuracy of the ice water content (IWC) derived from these datasets. However, there are basic measurement inaccuracies in 2D particle imagery that are inherent and contribute to uncertainties in determination of M . For example, Korolev et al. (1998) show from theoretical and laboratory work that 2D-C probe sizing errors of up to a factor of 2 can occur for particles of less than

150- μm size. Strapp et al. (2001) and Lawson et al. (2006a) show experimental results indicating that the response time of the 2D-C probe significantly limits its ability to properly size and even detect particles less than about 150 μm at airspeeds in excess of 100 m s^{-1} . Also, the spatial orientation of ice crystals can have an effect on the accuracy of IWC calculation. A quantitative assessment is well beyond the scope of this work, but a few qualitative comments may be considered of value. If the orientations of particles are disrupted as they pass through the imaging instruments and a preferred orientation is established, then measurements may be biased to an unknown degree. For example, if plates naturally fall with their c -axis parallel to the gravity vector and are flipped so that they are imaged along their a axis, the image aspect ratio will increase and the value of M computed from Part I_{CSP} or Part I_{Area} will decrease. On the other hand, relationships using only L will not be as affected. If ice particles are imaged in a random orientation, the computed M of individual particles may increase or decrease, depending on orientation and the algorithm being used.

In this paper, we compare the results of applying ice particle image-to-mass relationships from BF95, M90, H02, and Part I_{CSP} or Part I_{Area} . First, we compare the various image-to-mass relationships using a theoretical analysis of ideal columns with an assumed geometry. We also show comparisons of five relationships applied to datasets of ice crystals collected at the South Pole, and collected using research aircraft in midlatitude cirrus and arctic stratus clouds. There are no sufficiently accurate instrument standards (i.e., ground truth) available for measuring IWC from these research aircraft or on the ground at the South Pole. In the absence of a measurement standard, we cannot rigorously compute measurement uncertainties or demonstrate that any of the IWC results are more accurate than others. Also, the Part I analysis was based on the Mitchell et al. (1990) dataset that was collected at the surface in the Sierra Nevada, and this dataset may not be representative of crystal types found in other types of clouds. The only substantial evidence for improvement in IWC using Part I_{CSP} or Part I_{Area} comes from application to the expanded M90 dataset, which showed a reduced rms error in crystal mass of nearly 50% and a reduction in uncertainty in the exponent β in (1) (see Part I). We show comparisons of results from BF95, M90, H02, Part I_{CSP} , and Part I_{Area} applied to field data, however, to provide insights into the possible magnitudes of differences that can result from applying the five methods. The differences vary by up to a factor of 3, depending on the crystal shapes and sizes involved. For the sake of simplicity in this paper, we refer to results from meth-

TABLE 1. Values of parameters α and β for BF95 and M90 when $X = L$ in (1), for Part I_{Area} when $X = A$ in (1), and for Part I_{CSP} when $X = CSP$ in (1).

	M90	BF95	Part I_{CSP}	Part I_{Area}
α	0.022	0.037	0.135	0.115
β	2.000	1.900	0.793	1.218

ods based on BF95, M90, and H02 as under- or over-estimates when compared with Part I_{CSP} or Part I_{Area} .

2. Comparison of relationships applied to columns and spheres

In this section we compare results from relationships based on BF95, M90, Part I_{CSP} , and Part I_{Area} when applied theoretically to ideal columns and spheres. When applying M90, BF95, Part I_{CSP} , and Part I_{Area} , the mass of the circumscribed sphere assuming solid ice is used if it is less than the mass calculated with (1). For BF95 this occurs at $L < 100 \mu\text{m}$. For M90 this occurs at $L < 45.8 \mu\text{m}$. For Part I_{CSP} and Part I_{Area} , the value of L at which the computed mass exceeds the spherical

mass depends on particle shape, and ranges from approximately 30 to 100 μm . The values for α and β used in (1) for the comparisons shown in this paper are listed in Table 1. In (1), M is expressed in units of milligrams; X is expressed in units of millimeters for BF95 and M90, in units of cubic millimeters for Part I_{CSP} and in units of squared millimeters for Part I_{Area} . H02 use a power-law relationship that is a function of A and L . However, they combine these parameters together with M to form two new parameters—area ratio and effective density—and apply the power-law relationship to these parameters for various crystal types.

Figure 1 shows plots of M90, BF95, Part I_{CSP} , and Part I_{Area} column masses as a function of column length and aspect ratio in comparison with the mass computed for an ideal column. The mass of an ideal, solid column, when computed from a two-dimensional projection such as a 2D image, depends on its orientation in space and some assumptions concerning its geometry. The masses of columns in Fig. 1 were computed from column length, aspect ratio (L/W), and the assumption that the column is solid with all six prism faces of equal

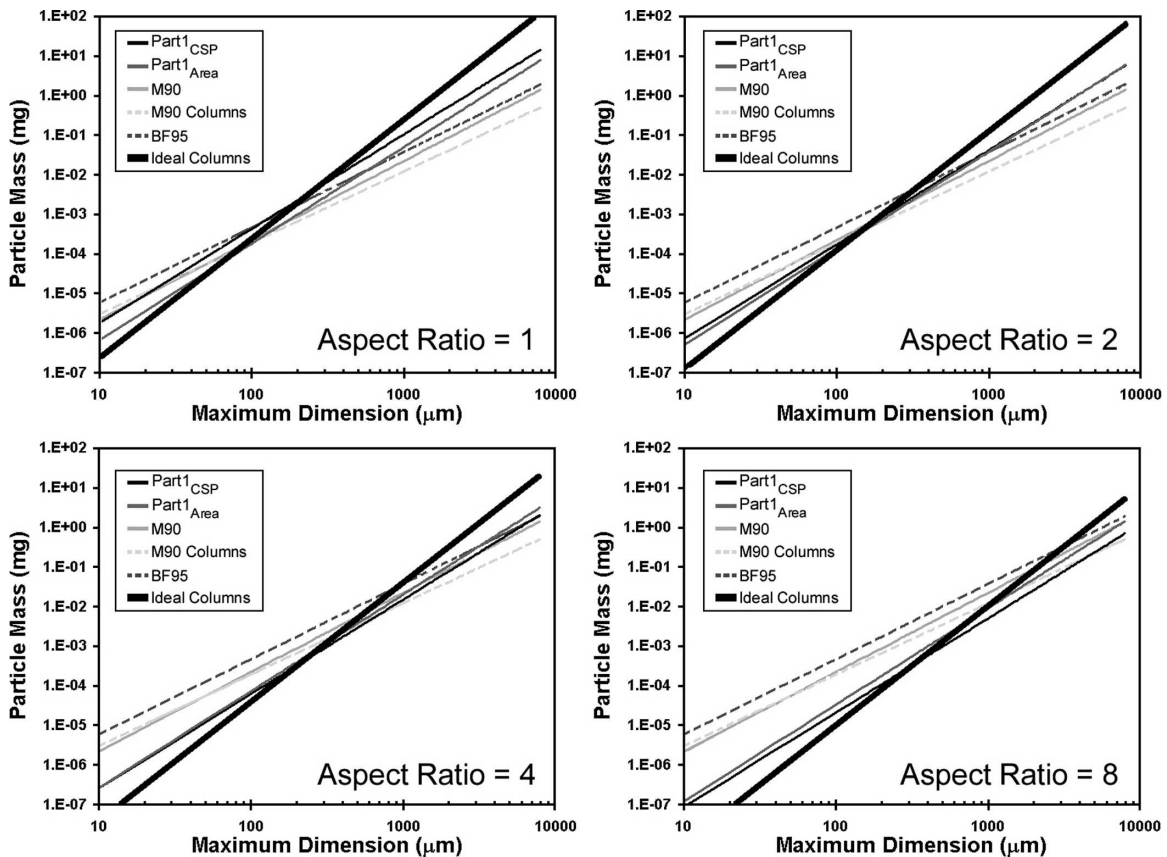


FIG. 1. Plots of particle mass estimates vs maximum particle dimension L for ideal columns at various aspect ratios. Various curves show results using the M90 general relationship, M90 specific to columns, BF95, and Part I_{CSP} and Part I_{Area} relationships. Also shown is the relationship for the actual mass of an ideal column.

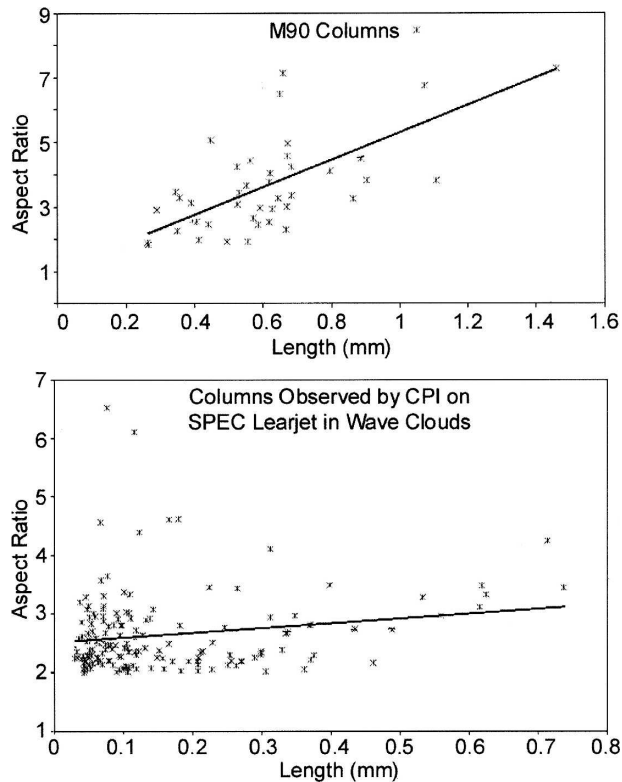


FIG. 2. Scatterplots of column aspect ratio vs length with linear regression line for (top) columns from the expanded M90 dataset and (bottom) wave clouds.

area. The development of formulas used to generate Fig. 1 and an estimate of errors in mass resulting from 2D images of columns that are randomly oriented in space is described in the appendix. Also contained in the appendix is a brief explanation of how our ideal column formula differs from that derived by H02.

The results using H02 are not shown in Fig. 1 because for aspect ratios < 8 , the maximum difference in their column-specific formula is 25% of that for an ideal column (see the appendix), and there is no discernable difference on a log-log plot such as Fig. 1. Both the BF95 and M90 curves cross the curve for the actual column mass at fairly sharp angles; the value of L where they cross increases with increasing aspect ratio. Interestingly, the M90 relationship that is habit specific for columns performs slightly worse than the M90 average relationship. This is because, as shown in Fig. 2, the typical aspect ratio of columns analyzed in the expanded M90 dataset increased with L from approximately two at $L = 300 \mu\text{m}$ to 6 at $L = 1.2 \text{ mm}$. If the aspect ratio-to-length relationship in the expanded M90 dataset were universally true for columns, then the M90 column-specific relationship would be applicable, despite the apparent disagreement shown in Fig. 1 for

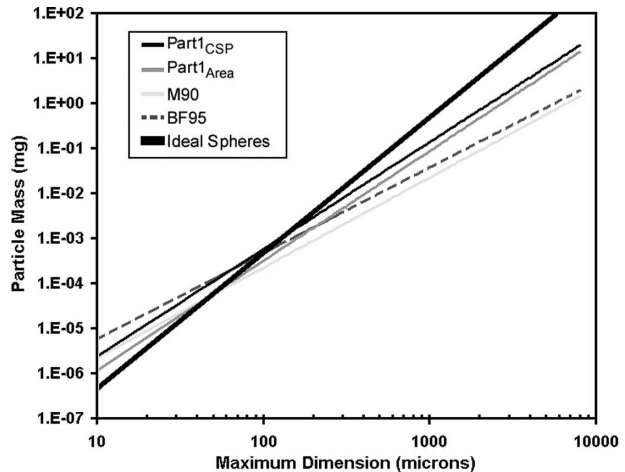


FIG. 3. As in Fig. 1, except plots are for an ideal sphere.

fixed aspect ratios. However, the scatter in the data suggests otherwise, as does the column data in Fig. 2 that were collected in wave clouds by the SPEC, Inc., Learjet. The wave cloud data suggest that the typical column aspect ratio does not always change with L in the manner observed in the expanded M90 dataset.

Ono (1969) and Auer and Veal (1970) also measured the length and aspect ratio of natural ice crystals. While they did not find that the aspect ratio tended to 2, they did find aspect ratio-to-length relationships that differed from the expanded M90 dataset. The point to be made here is that the aspect ratio-to-length relationship in the expanded M90 dataset is not universal and therefore cannot be expected to apply to all datasets containing columns. The $\text{Part } I_{\text{CSP}}$ relationship, on the other hand, incorporates L , W , A , and P , which tends to compensate for changes in aspect ratio. $\text{Part } I_{\text{Area}}$ performs almost as well as $\text{Part } I_{\text{CSP}}$. As shown in Fig. 1, the slopes of the $\text{Part } I_{\text{CSP}}$ and $\text{Part } I_{\text{Area}}$ lines are both closer to the slope of the actual mass line than M90 and BF95. Therefore $\text{Part } I_{\text{CSP}}$ and $\text{Part } I_{\text{Area}}$ should have less overall error than M90 and BF95 when applied to real data.

Spherical particles are the opposite geometric extreme of crystals with large aspect ratios, such as columns, because the aspect ratio of a sphere is equal to one, which is the minimum possible. Figure 3 shows plots in the same format as Fig. 1, except applied to an ideal spherical particle. Again, the $\text{Part } I_{\text{CSP}}$ formula provides the best overall approximation to the mass of an ideal sphere. The $\text{Part } I_{\text{Area}}$ curve is closest to $\text{Part } I_{\text{CSP}}$. The M90 and BF95 curves compare well within the size range from about 50 to 300 μm and diverge significantly from the actual mass outside of that size range.

Based on the plots shown in Figs. 1 and 3, it can be

seen that Part I_{CSP} should provide the best overall estimates of mass for spherical particles and for columnar particles. Part I_{Area} performs almost as well as Part I_{CSP} , with the largest differences observed with an aspect ratio of 1. M90 and BF95 perform well only within limited size ranges and aspect ratios. Also, since Part I_{CSP} is formulated based on a physical concept whereby L , W , A , and P are used to compensate for variations in crystal shape, and it was statistically derived from real ice particle data, we expect that Part I_{CSP} will perform better when applied to datasets of actual ice crystals.

3. Comparison of relationships in natural clouds

Here we discuss the results of applying IWC algorithms based on M90, BF95, H02, Part I_{CSP} , and Part I_{Area} relationships to datasets collected in field campaigns. IWC is computed in the standard way by dividing the accumulated ice crystal mass by the volume of air containing the crystals. It is important to reiterate here that, because there is no IWC measurement standard, there is no way to quantitatively compare the IWC results from each relationship. Therefore, we speak in terms of “differences,” not measurement errors. For the sake of brevity, differences from the Part I_{CSP} result are referred to as over- (+) and under- (–) estimates. Where appropriate, we interpret the results of the field data in terms of the trends seen in Figs. 1 and 3; that is, the various relationships are compared with their performance when applied to ideal columnar and spherical ice particles.

The first dataset that is discussed was collected by a cloud particle imager (CPI) on the ground at the South Pole and the second dataset was collected in clouds using research aircraft. The crystals observed at the South Pole fell a very short distance from clouds that were within 1 km of the ground; the crystals were formed at the cold temperatures typically observed in cirrus clouds. The South Pole crystals are typically pristine and unrimed and relatively uniform in shape, and, unlike the dataset collected by research aircraft, the South Pole dataset contained an insignificant amount of small spheroidal and irregularly shaped crystals. A disadvantage of the South Pole dataset is that the crystal size rarely exceeded 300 μm in length.

In situ cloud particle data were collected by the SPEC Learjet research aircraft in midlatitude cirrus clouds, and by a C-130 research aircraft operated by the National Center for Atmospheric Research (NCAR) in a deep Arctic stratus cloud. The data contain ice particles measured by a forward-scattering spectrometer probe (FSSP) described by Knollenberg (1981), a CPI described by Lawson et al. (2001), and 2D-C and 2D-P

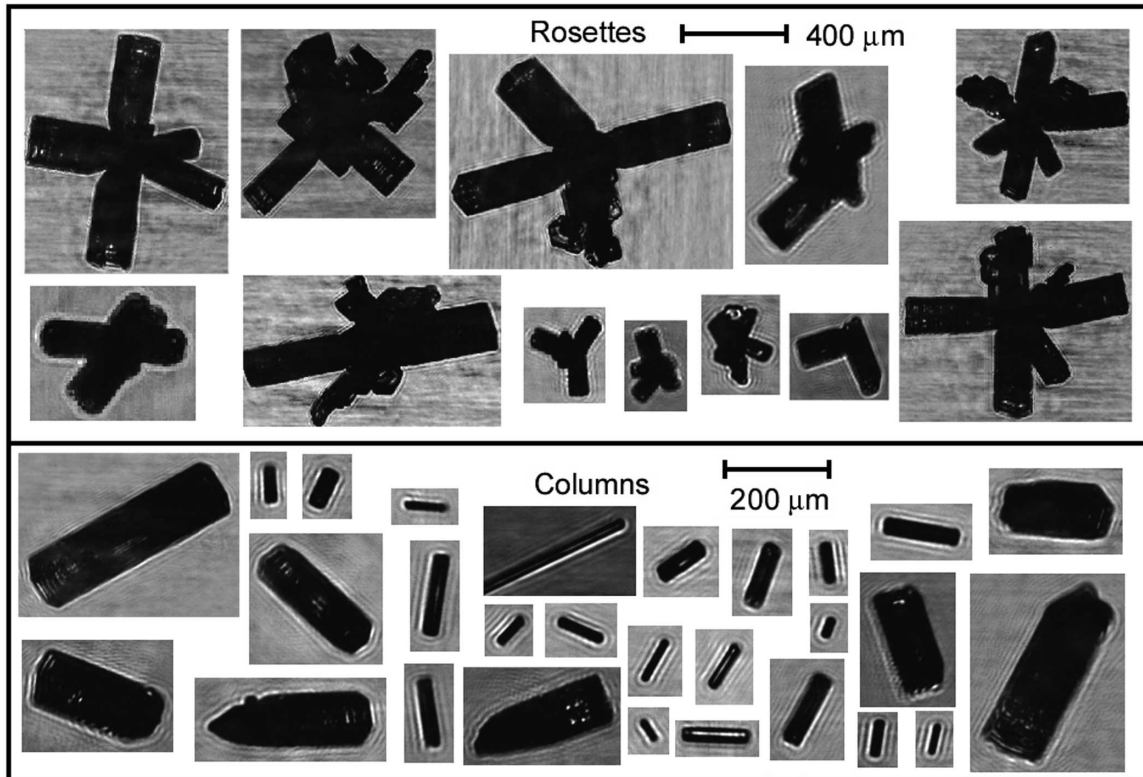
probes. Nominally, the FSSP measures particles in the size range from 3 to 45 μm , the CPI from 7 to 2000 μm , the 2D-C from 75 μm to about 1 mm, and the 2D-P from 1 mm to about 1 cm, depending on how the images are processed.

In this analysis, measurements from the particle probes are combined into a composite particle size distribution (PSD) using a technique described by Lawson et al. (2001). Basically, “break points” are chosen on a case-by-case basis so that the combined PSD is as continuous as possible and the sampling statistics of each probe are optimized. The sizes of crystals in these clouds ranged from approximately 3 μm to in excess of 1 cm.

All FSSP data are assumed to be spherical ice particles. CPI particles are only processed when less than 6% of the image has been truncated as a result of being out of the field of view. Two-dimensional images recorded by the SPEC Learjet were processed in the same way as CPI images, that is, using a cutoff value of 6% and Part I_{CSP} . Two-dimensional images recorded by the NCAR C-130 were processed using the “center in” technique described by Heymsfield and Parrish (1978). Part I_{CSP} is applied to CPI data and 2D data when L , W , A , and P are available, which was always the case except for the NCAR C-130 2D data, because L , W , and P are not available in the C-130 dataset. In the case of the C-130 2D data, Part I_{Area} is used. Part I_{Area} is also applied to the Learjet CPI and 2D data for the sake of comparison. For CPI and Learjet 2D data, L , W , A , and P are computed as described in Part I. For the NCAR C-130 2D data, L is the maximum dimension in the direction of particle flow or perpendicular to particle flow and A is determined from the number of occulted pixels. For both Learjet and C-130 2D data, the sample area of the 2D probes is corrected for depth of field using the relationships given in the Particle Measuring Systems, Inc., (PMS) operator’s manual. The sample area of the CPI was corrected using an empirical relationship that decreases the sample area of particles $< 100 \mu\text{m}$ as a function of A .

Figure 4 shows examples of ice crystals imaged by a CPI at the South Pole and IWC calculations using the M90, BF95, H02, and Part I_{CSP} and Part I_{Area} relationships. The percentage differences in IWC shown in Fig. 4 are computed using the formulas shown in the tabular portion of the figure, and indicate the differences between Part I_{CSP} in comparison with M90, BF95, and H02, and Part I_{Area} in comparison with M90, BF95, and H02. Figure 5 shows PSDs based on number concentration and particle mass for columnar and bullet rosette ice crystals shown in Fig. 4.

The crystal images shown in Fig. 4 were automati-



	IWC (g m ⁻³)				
	Part1 _{CSP}	Part1 _{Area}	M90	BF95	H02
Rosettes	0.0132	0.0120	0.0104	0.0203	0.0115
Columns	0.0518	0.0657	0.1566	0.2119	0.0380

	Percentage Difference in IWC					
	$100 \left(\frac{M90 - \text{Part1}_{CSP}}{\text{Part1}_{CSP}} \right)$	$100 \left(\frac{BF95 - \text{Part1}_{CSP}}{\text{Part1}_{CSP}} \right)$	$100 \left(\frac{H02 - \text{Part1}_{CSP}}{\text{Part1}_{CSP}} \right)$	$100 \left(\frac{M90 - \text{Part1}_{Area}}{\text{Part1}_{Area}} \right)$	$100 \left(\frac{BF95 - \text{Part1}_{Area}}{\text{Part1}_{Area}} \right)$	$100 \left(\frac{H02 - \text{Part1}_{Area}}{\text{Part1}_{Area}} \right)$
Rosettes	-22%	53%	-13%	-13%	70%	-4%
Columns	203%	309%	-27%	138%	222%	-42%

FIG. 4. Examples of (top) rosette and columnar CPI images of ice crystals observed at the South Pole, and (bottom) values of IWC and percentage differences computed using M90, BF95, H02, and Part I_{CSP} and Part I_{Area} relationships.

cally sorted into particle habit categories by CPIview software, a program developed by SPEC for this purpose. Thus, the values of IWC shown are for the sorted dataset and are not representative of IWC in the atmosphere, because irregular and other shapes that did not meet the habit classification criteria have been eliminated. Several features of the images are used to classify the habit of the images, including aspect ratio, perimeter-to-area ratio, and radial harmonics, which are derived from a Fourier analysis of a series of radii drawn from the image centroid to its perimeter. More detailed information concerning the crystal habit classification software can be found in Baker and Lawson

(2006b) and Lawson et al. (2006b,c). A visual inspection of the results of the crystal classification program, when applied to the crystals analyzed in this paper, indicates that classification reliability is greater than 90%.

Figure 4 shows distinct trends that can mostly be predicted from the results of Figs. 1, 3, and 5. The comparison of Part I_{CSP} and Part I_{Area} with M90 and BF95 shows that both M90 and BF95 overestimate the IWC of columns when compared with Part I_{CSP} and Part I_{Area} by large amounts, ranging from a factor of 2 to 3. This can be explained by examination of Figs. 1 and 5. Figure 5 shows that the mass PSD peaks around 60 μm

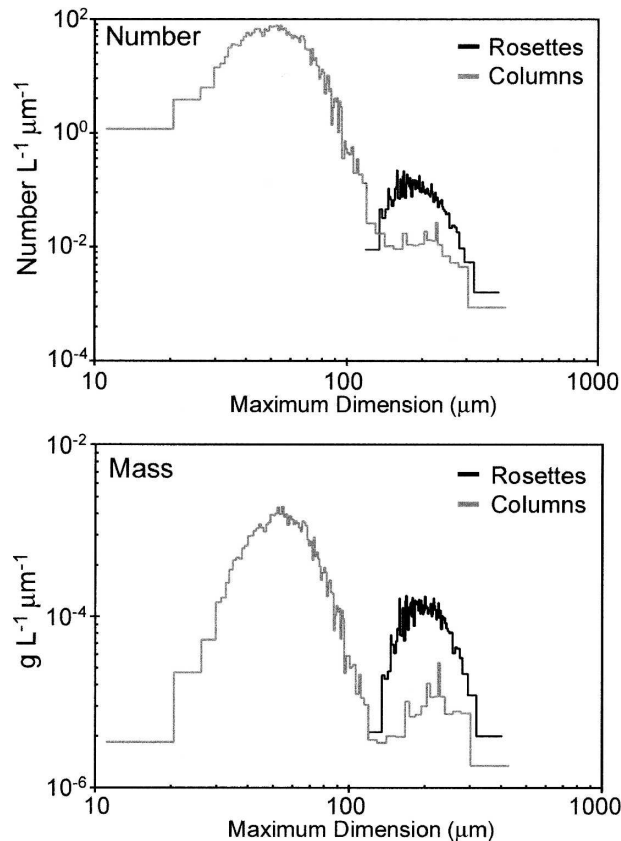


FIG. 5. Particle size distributions as a function of (top) number and (bottom) mass for columnar and rosette ice crystals observed with a ground-based CPI at the South Pole. Examples of CPI images of columns and rosettes are shown in Fig. 4.

(which corresponds to the pristine columns seen in Fig. 4) and again from 200 to 300 μm (which corresponds to the bullets and large columns). The aspect ratio of these columns varies from about 2 for the bullets and larger columns to about 4 for the smaller columns. Based on Fig. 1, it can be seen that both M90 and BF95 overestimate mass in this size range by about an order of magnitude when compared with the ideal column mass, and almost as much when compared with Part I_{CSP} and Part I_{Area} . In comparison, H02, which reduces to nearly the ideal column formula for this aspect ratio, only differs from Part I_{CSP} and Part I_{Area} by -27% and -42% , respectively.

A comparison of IWC values for rosettes in Fig. 4 shows better agreement between both M90 and BF95 when compared with either Part I_{CSP} or Part I_{Area} . This can be explained by examination of Figs. 3 and 5. Rosettes are closer to a spherical shape than columns, although their mass is still substantially less than an equivalent sphere computed using L . Based on Fig. 3, it can be seen that the M90 curve is substantially less than

any of the other curves in the size range from about 150 to 300 μm , which corresponds with the peak in rosette mass in Fig. 5. The IWC values in Fig. 4 show that the M90 value is less than both Part I_{CSP} and Part I_{Area} , by -21% and -13% , respectively, which is considerably improved over the columns comparison. Figure 4 shows that BF95 IWC values are $+54\%$ and $+69\%$ larger than Part I_{CSP} and Part I_{Area} . Because the BF95 curve in Fig. 3 gives IWC values that are about a factor of 2 higher than M90 in the 150–300- μm size range, it is expected that BF95 will produce considerably larger values of IWC than M90. On the other hand, both Part I_{CSP} and Part I_{Area} use a projected image area in the mass calculation, so the IWC values from these relationships are less than that for the ideal sphere shown in Fig. 3 and fall between the values for M90 and BF95 in Fig. 4. H02 also uses projected area in the calculation of mass, and in this case where the ice crystal population is composed almost entirely of rosettes, the H02 rosette IWC compares well with both Part I_{CSP} and Part I_{Area} .

Figure 6 shows examples of particle images collected by 2D-C and CPI probes in midlatitude cirrus and Arctic stratus clouds, along with IWC computed using M90, BF95, and Part I_{CSP} and Part I_{Area} . The 2D-P images are also used in the dataset collected by the NCAR C-130 aircraft in Arctic stratus clouds and were used for $L > 1$ mm in this study. Corresponding particle size distributions for each of the cases in Fig. 6 are shown in Fig. 7. Unlike the data in Fig. 4, where the CPI images were sorted by crystal habit and include only particles up to the maximum crystal size of about 300 μm , the IWCs in Fig. 7 are calculated using all of the particles observed during the cloud pass. Typical images are shown for each cloud pass. All of the cloud passes contain relatively high concentrations of small (< 50 μm) spheroidal particles and (except for the cirrus at -55°C) irregularly shaped particles ranging from approximately 50 to 200 μm in size, as shown in Figs. 6 and 7.

Although the error trends based on aspect ratio and L shown in Figs. 1 and 3 are specific to columnar and spherical shapes, we again draw upon trends seen in these figures to explain the IWC comparisons shown in Fig. 6. The numbered entries in Fig. 6 will be discussed starting at the top of the figure and proceeding downward.

Entries 1 and 2 are taken from composite PSDs based on Learjet flights in midlatitude cirrus, as described in Lawson et al. (2006b). Entry 1 shows data collected in a midlatitude cirrus cloud at -55°C . The CPI images are mostly of small, spherical particles with an occasional budding rosette or irregularly shaped particle. The PSDs in Fig. 7 show that the large majority of

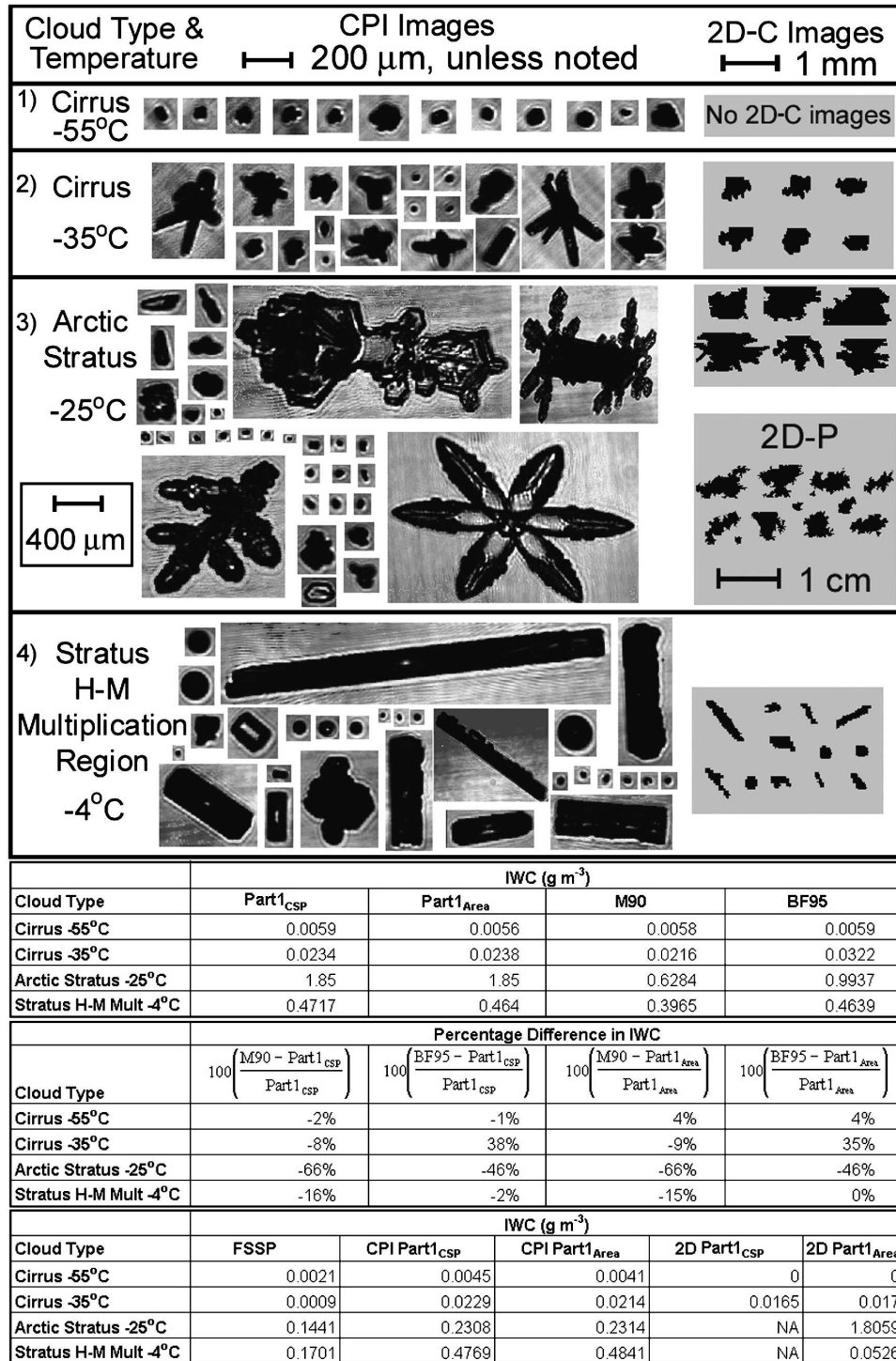


FIG. 6. Examples of (top) ice crystals observed by research aircraft, and (bottom) values of IWC, percentage differences computed using M90, BF95, H02, and Part I_{CSP} and Part I_{Area} relationships, and IWC computed using individual probes.

the mass is contained in sizes near 30–40 μm and the largest particles do not exceed about 150 μm. As expected (Lawson et al. 2006a), the 2D-C probe does not image any of these particles at the Learjet airspeed of

180 m s⁻¹. In this case, M90, BF95, and Part I_{CSP} and Part I_{Area} all produce about the same values of IWC, because all of the relationships reduce to a spherical mass formula for particles in the 20–40-μm size range.

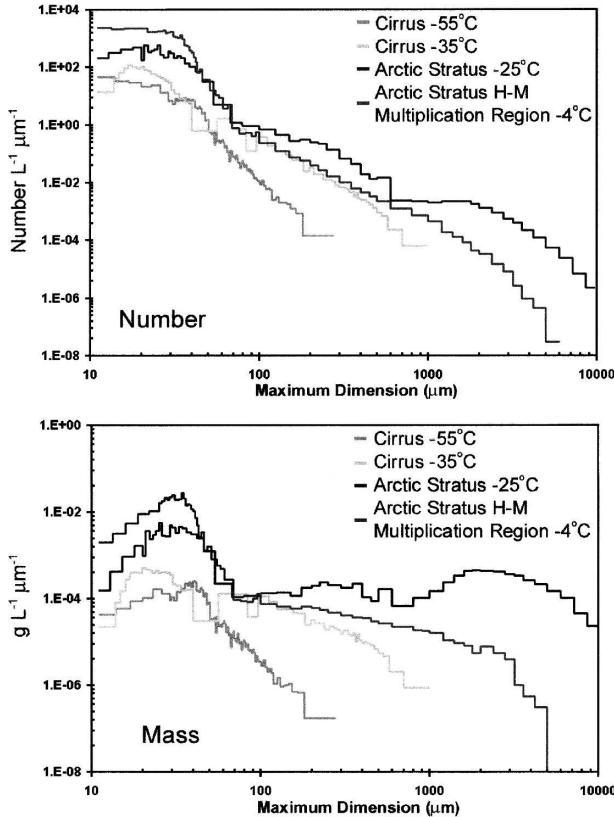


FIG. 7. Particle size distributions as a function of (top) number and (bottom) mass for the four cases shown in Fig. 6.

Thus, for clouds that exhibit this range of small particles, there is no clear advantage to using one relationship over another.

Figure 7 shows that the mass of particles observed in midlatitude cirrus at -35°C (entry 2) extend out to 1 mm, which is much larger than the particles found at -55°C (entry 1) in midlatitude cirrus. The images in entry 2 in Fig. 6 show that most of these particles are small spheroids, small rosettes, and irregulars. The average aspect ratio of the particles is 1.3:1. Figure 3 shows that in the size range from 100 to 1000 μm , BF95 gives a mass that is about 2–5 times that of M90. When compared with Part I_{CSP} and Part I_{Area} , respectively, the data in Fig. 6 suggest that BF95 is overestimating mass by 35%–39% and M90 is underestimating mass by -8% to -9% . This is the same trend seen in the rosette South Pole data shown in Fig. 4. However, there is a peak in the midlatitude cirrus mass PSD from about 20 to 30 μm , and because all four relationships reduce to a spherical formula, this tends to mitigate the over- and underestimates by BF95 and M90 at the larger particle sizes.

Entry 3 in Fig. 6 shows data for a deep Arctic stratus cloud that were collected on 18 July 1998 by the NCAR

C-130 aircraft during the First International Satellite Cloud Climatology Project (ISCCP) Regional Experiment (FIRE) Arctic Cloud Experiment (ACE) (Curry et al. 2000). Figure 7 shows that in this case the PSD contains high mass concentrations of particles in the size range from 100 μm to 1 cm. Even though there is a peak in mass from 20 to 50 μm , the amount of mass in particle sizes $>100 \mu\text{m}$ is an order of magnitude larger. As shown in the typical images in Fig. 6, the aspect ratios of the particles ranged from about 1 to 2. Based on Figs. 1 and 3, both M90 and BF95 tend to grossly underestimate mass at a relatively low aspect ratio and large particle size. Figure 6 shows that M90 and BF95 underestimate IWC by a factor of 2–3 when compared with Part I_{CSP} and Part I_{Area} .

Entry 4 shows measurements from the same Arctic stratus cloud as in entry 3, but in a region where there was Hallett–Mossop (H–M) ice multiplication with mostly large columns with high aspect ratios and concentrations of ice crystals $<50 \mu\text{m}$ that exceeded 2000 L^{-1} (Lawson et al. 2001). As seen in Fig. 1, in the size range from 100 to 1000 μm and at aspect ratios that increase from 2 to 8, the trend is for M90 and BF95 to transition from an underestimate to an overestimate of IWC of columnar crystals as aspect ratio increases. Figure 3 shows that there is a tendency for both M90 and BF95 to overestimate the mass of spheres at sizes $<50 \mu\text{m}$. Also, the BF95 relationship changes to a spherical formula at $L < 100 \mu\text{m}$ and M90 transitions to spheres at $L < 45.8 \mu\text{m}$. The combination of these (offsetting) effects produces average M90 and BF95 estimates of IWC that are in good agreement with the value produced using the Part I_{CSP} and Part I_{Area} relationships.

The results from entries 3 and 4 in Figs. 6 and 7 indicate that when the particle size distribution extends to large particle sizes, the BF95 and M90 relationships tend to significantly underestimate IWC when compared with Part I_{CSP} and Part I_{Area} . However, if the large portion of the PSD is dominated by particles with a large aspect ratio and there are high concentrations of very small (spherical) particles, this tendency may be mitigated and M90 and BF95 relationships can be found to be in reasonably good agreement with Part I_{CSP} and Part I_{Area} .

The effects of possible shattering of large ice crystals on the inlets of particle probes has been discussed by several investigators (Gayet et al. 2002; Field et al. 2003; Lawson et al. 2006b; Korolev and Isaac 2005) and has raised concern that crystal shattering could be producing high concentrations of small particles. The large tails and relatively high concentrations of small ice particles seen in the PSDs in entries 3 and 4 in Fig. 7 could potentially be a result of crystal shattering. While ex-

amination of the effects of crystal shattering is beyond the scope of this paper, it should be pointed out that it could potentially have some effect on the calculation of IWC from particle probes. Results from Korolev and Isaac (2005) suggest that the number of shattered crystals generated is less than about 10%, except possibly in regions with high concentrations of large dendrites. Field et al. (2003) suggest that the FSSP concentration could be increased by a factor of 2 as a result of crystal shattering. While the actual IWC in the atmosphere is not altered by particle shattering, particle probe measurements and the algorithms used to compute IWC might be influenced by particle shattering. In the three cases reported in Fig. 6 where particles are large enough to contribute to shattering (entries 2, 3, and 4), the contribution of mass from the small particles is a small fraction relative to that from the larger particles, so shattering is not a significant issue.

Results discussed in this section suggest that, if, for the sake of comparison, one assumes the values computed using the Part I_{CSP} and Part I_{Area} relationship are correct, then significant (greater than a factor of 2) errors in IWC can arise from using M90 and BF95 IWC relationships. Based on a comparison of performance of the M90, BF95, and Part I_{CSP} and Part I_{Area} relationships applied to ideal columns and spheres, it is possible to predict general trends of under- and overestimation of IWC from particle sizes and aspect ratios. However, no attempt was made here to develop a quantitative technique for adjusting M90 and BF95 results. Instead, we suggest that users reprocess original datasets using the Part I_{CSP} or Part I_{Area} techniques and then qualitatively compare with previous results based on analysis of the PSDs and aspect ratios.

There is no way to quantitatively evaluate the improvement of the Part I_{CSP} and Part I_{Area} IWC relationships in comparison with M90 and BF95 using actual airborne measurements, because there was no standard for measuring IWC from these research aircraft. Even more direct techniques that relate mass to the measurement of the ice vaporization process (e.g., Twohy et al. 1997; Korolev et al. 1998) are subject to uncertainties that are not well quantified. While remote (e.g., radar) measurements of ice mass are also fraught with uncertainties, the vertical trends of radar and in situ measurements are useful for comparison. For example, Zuidema et al. (2005) found that the vertical profile of IWC computed using Part I_{CSP} compared better with radar-derived IWC than the BF95 IWC in an Arctic stratus cloud. However, far more comparisons in varying conditions are required to demonstrate that one relationship is more accurate than the other.

4. Summary and discussion

Part I expanded the M90 dataset of photographed ice particles and melted drops and derived two new relationships for M . They demonstrate that, when applied to the expanded M90 dataset, using a combined single parameter (CSP) relationship that is a function of L , W , A , and P in place of L alone results in a reduction of nearly 50% in the RMS error in M . A second relationship using A alone resulted in the same magnitude of error reduction. A comparison of the M90, BF95, and Part I_{CSP} and Part I_{Area} relationships for spheres and ideal columns with various aspect ratios shows that, when compared with the Part I_{CSP} and Part I_{Area} relationships, both M90 and BF95 tend to overestimate the mass of smaller columns and underestimate the mass of larger columns. The crossover point where the overestimate changes to an underestimate increases with aspect ratio, shifting from approximately $100 \mu\text{m}$ at 1:1 to approximately 1 mm at 6:1.

The Part I_{CSP} and Part I_{Area} relationships were compared with M90 and BF95 using ice particle data collected by a CPI at the surface at the South Pole and by CPI and 2D probes on research aircraft in midlatitude cirrus and a deep Arctic stratus cloud. The ice crystals at the South Pole provided datasets of columns and rosettes with particle sizes up to $\sim 300 \mu\text{m}$. For the sake of comparison, the IWC of columns and rosettes was also calculated using a relationship developed by H02 that incorporates particle area and maximum particle dimension. For the most part, the H02 relationship produced column and rosette IWC values that were much closer in value to Part I_{CSP} and Part I_{Area} than M90 and BF95, which is expected because H02 incorporates A and L . However, because the H02 relationships are habit specific, they could not be applied with confidence to data collected by research aircraft in clouds, which generally contain mostly irregular crystals (Korolev et al. 1999; Baker and Lawson 2006b; Lawson et al. 2006b).

Comparison of Part I_{CSP} and Part I_{Area} with M90 and BF95, when applied to the data collected in or falling from natural clouds, indicates that results using the M90 and BF95 relationships differ from Part I_{CSP} and Part I_{Area} by up to a factor of 3, depending on particle size and shape. The direction of the differences, that is, either the under- or overestimate of IWC, depends on particle size and aspect ratio. In the upper parts of midlatitude cirrus clouds with temperatures of -55°C , where the particle types are mostly small spheroidal particles and budding rosettes $< 150 \mu\text{m}$, differences in IWC using BF95 and M90 relationships are negligible when compared with Part I_{CSP} and Part I_{Area} . However,

as particle sizes increase, especially for low aspect ratios, the magnitude of the difference increases significantly. In clouds where the majority of the mass is contained in particles from 100 μm to 1 cm and aspect ratios $<2:1$, the M90 and BF95 relationships tend to underestimate IWC by approximately a factor of 2–3. On the other hand, if the particle size distribution contains high concentrations of small ($\sim 50 \mu\text{m}$) particles and/or large particles with high ($>4:1$) aspect ratios, the individual errors in each of these size ranges have opposite signs and IWC from the M90 and BF95 relationships are in better agreement with Part I_{CSP} and Part I_{Area} .

A noteworthy feature of the Part I_{Area} relationship is that it can be applied to existing, archived datasets of 2D-C and 2D-P images, provided that the number of occulted pixels in each image, that is, projected area, is available.

Acknowledgments. This work was performed under funding from National Science Foundation ATM-9904710, NSF ATM-0244731, NSF OPP-0084314, NASA TRMM NAS5-00244, and NASA NNG04GE71G.

APPENDIX

Derivation of Formulas for Computing the Mass of an Ideal Solid Column

This appendix defines the basic geometry and develops equations used to create Fig. 1 in the main part of this paper. It also contains an estimate of how much error can be expected when a specific column orientation is assumed, as compared with masses computed from 2D projections that are randomly orientated in space.

Figure A1 shows a three-dimensional perspective drawing of an ideal solid column, which is defined by two parameters, here chosen as L' and a . Figure A2 shows two projections of the hexagonal column onto a two-dimensional plane. One is an end view and the second is a side view. Coordinate axis and further variables are also defined in this figure. Respectively, L and W are the lengths of the maximum chord and the maximum perpendicular chord as defined in the main text as length and width; L' and W' are the customary length and width of a rectangle.

The mass of an ideal ice column is the bulk density of ice ($\rho_b = 0.917 \text{ g cm}^{-3}$) times the volume V of the crystal, or

$$V = \frac{3\sqrt{3}}{2} a^2 L'. \tag{A1}$$

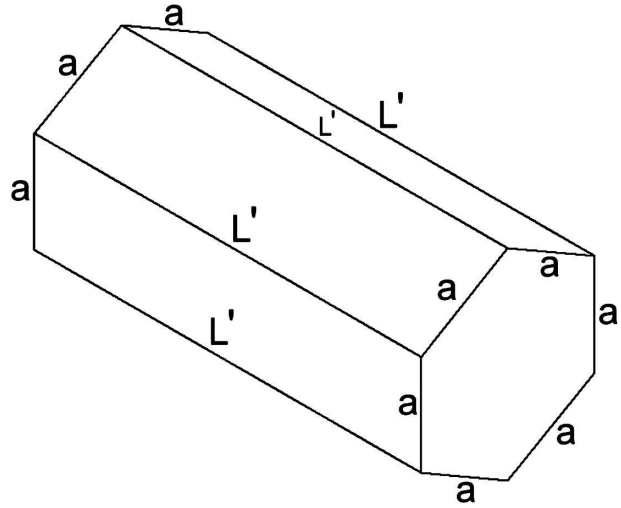


FIG. A1. Three-dimensional perspective drawing of an ideal, solid column as a hexagonal column.

The mass estimated from a 2D image, however, is based on a two-dimensional projection of the column. Both L and W depend on orientation of the crystal relative to a two-dimensional plane. First, consider rotation of a side view of the column about the z axis (Fig. A2). This rotation causes no change in the image because the axis of rotation is perpendicular to the plane of projection. Next, it can be seen from Fig. A2 that rotation of the column about its x axis, while maintaining a rectangular side view projection, causes the values of L , W , and W' to vary slightly for a fixed crystal (fixed values of L' and a). That is,

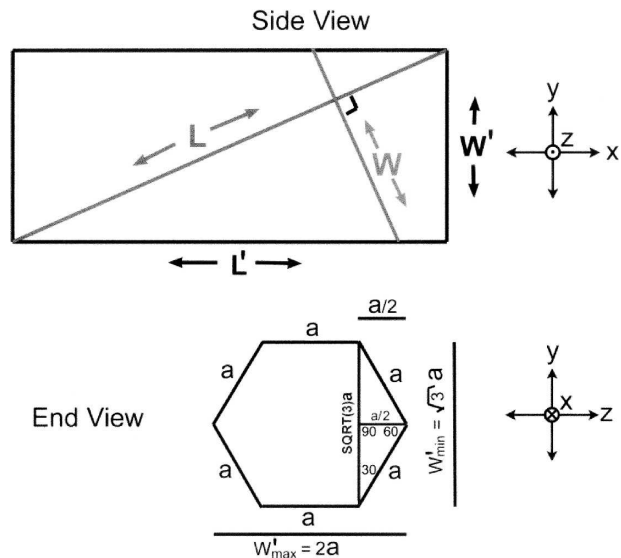


FIG. A2. Side view and end view projections of an ideal hexagonal column onto a two-dimensional plane. Coordinate axis and other variables discussed are defined pictorially.

TABLE A1. Values of L/L_{sv} for a range of aspect ratios.

r_a	1	2	3	4	5	6	7	8	9	10
L/L_{sv}	0.94	0.86	0.81	0.77	0.75	0.73	0.72	0.71	0.70	0.70

$$W' = f_1 \left(\frac{\sqrt{3} + 2}{2} \right) a, \quad (\text{A2})$$

where $0.93 < f_1 < 1.07$.

Because W' is squared in the volume calculation, the 7% uncertainty yields a 15% uncertainty in volume and mass estimates for any given crystal. However, for an IWC based on an ensemble of randomly oriented columnar crystals, these errors cancel and the uncertainty becomes small.

For a side view projection of a columnar crystal, (A1) may be rewritten in terms of L and aspect ratio ($r_a \equiv L/W = L'/W'$) by taking $f = 1$, or

$$V = \frac{3\sqrt{3}L^3}{2r_a^2} \left(\frac{r_a^2}{r_a^2 + 1} \right)^{3/2}. \quad (\text{A3})$$

Equation (A3) was used for the ideal column mass calculation in producing Fig. 1 in the main part of this paper. Figure 1 compares various estimated masses and the masses of ideal columns as functions of L for various aspect ratios. The independent variable for Fig. 1 is L . The M90 and BF95 estimates depend directly on L ; H02 also includes A ; Part I_{Area} uses A alone and Part I_{CSP} uses L , A , P , and W . For the side view ideal column geometry all of these additional terms can be found in terms of L and r_a , which can be expressed as

$$W = \frac{L}{r_a}, A = \frac{L^2}{r_a} \left(\frac{r_a^2}{r_a^2 + 1} \right), \text{ and } P = 2L \frac{r_a + 1}{\sqrt{r_a^2 + 1}}. \quad (\text{A4})$$

The mass estimates for M90, BF95, H02, Part I_{Area} , and Part I_{CSP} shown in Fig. 1 are computed using (A4).

The error resulting from rotation about the y axis is now considered. In this case the two-dimensional projection of an ideal column is no longer rectangular. However, L and W are still well defined as the longest chord and the longest perpendicular chord, respectively. Column volume and thus mass depend linearly on L , so the error in crystal mass can be estimated by evaluation of the change in L as the crystal is rotated. The exact value of L depends also on the angle of rotation about the x axis as well as about the y axis. However, the uncertainty resulting from rotation about the x axis is significantly less even than the 7% discussed above for W' , and is also subject to cancellation for a random ensemble of orientations. Thus, rotation about

the x axis will be ignored, which is analogous to assuming the hexagonal column is a cylindrical column.

Let θ be the angle of rotation about the y axis, that is, the angle that the long axis of the crystal makes with the two-dimensional plane of projection. Let L_{sv} be the side view L from Fig. 2. Then,

$$L = L_{sv} \times \text{Max}[\cos(\theta - \phi), \cos(\phi)\sqrt{\cos^2(\theta) + r_a^{-2}}], \quad (\text{A5})$$

where $\phi = \tan^{-1}(r_a^{-1})$. Table A1 shows the average value of L/L_{sv} for various values of r_a when L/L_{sv} is averaged over all possible angles. Table A1 shows that rotation of the side view of an ideal column about the y axis results in a 6% error in mass for $r_a = 1$ and increases to 30% error for $r_a = 10$.

H02 also derived equations for ideal hexagonal columns. They assumed a fixed side view orientation and derived an equation analogous to (A3) with $f = 1.07$. H02 rewrite that equation into their standard form of a power-law relationship between effective density and area ratio. This step is not exact;^{A1} however, it is a good approximation for aspect ratios between 2 and 8. The error between the ideal side view column mass and the side view column mass computed using the H02 formulation is 25% for $r_a = 1$, 8% for $r_a = 2$, 5% for $r_a = 4$, and 9% for $r_a = 8$.

REFERENCES

- Auer, A. H., Jr., and D. L. Veal, 1970: The dimensions of ice crystals in natural clouds. *J. Atmos. Sci.*, **27**, 919–926.
- Baker, B. A., and R. P. Lawson, 2006a: Improvement in determination of ice water content from two-dimensional particle imagery. Part I: Image-to-mass relationships. *J. Appl. Meteor. Climatol.*, **45**, 1282–1290.
- , and —, 2006b: In situ observations of the microphysical properties of wave, cirrus, and anvil clouds. Part I: Wave clouds. *J. Atmos. Sci.*, in press.
- Brown, P. R. A., and P. N. Francis, 1995: Improved measurements of the ice water content in cirrus using a total-water probe. *J. Atmos. Oceanic Technol.*, **12**, 410–414.
- Curry, J. A., and Coauthors, 2000: FIRE Arctic Clouds Experiment. *Bull. Amer. Meteor. Soc.*, **81**, 5–29.
- Davis, C. I., 1974: The ice-nucleating characteristics of various AgI aerosols. Ph.D. dissertation, University of Wyoming, 267 pp.

^{A1} There is no exact power-law relationship between effective density and area ratio for an ideal hexagonal column shape.

- Field, P. R., R. Wood, P. R. A. Brown, P. H. Kaye, E. Hirst, R. Greenaway, and J. A. Smith, 2003: Ice particle interarrival times measured with a fast FSSP. *J. Atmos. Oceanic Technol.*, **20**, 249–261.
- Gayet, J.-F., and Coauthors, 2002: Quantitative measurement of the microphysical and optical properties of cirrus clouds with four different in situ probes: Evidence of small ice crystals. *Geophys. Res. Lett.*, **29**, 2230, doi:10.1029/2001GL014342.
- Heymsfield, A. J., and J. L. Parrish, 1978: A computational technique for increasing the effective sampling volume of the PMS 2-D particle size spectrometer. *J. Appl. Meteor.*, **17**, 86–103.
- , S. Lewis, A. Bansemmer, J. Iaquina, L. M. Miloshevich, M. Kajikawa, C. Twohy, and M. R. Poellot, 2002: A general approach for deriving the properties of cirrus and stratiform ice cloud particles. *J. Atmos. Sci.*, **59**, 3–29.
- Knollenberg, R. G., 1970: The optical array: An alternative to scattering or extinction for airborne particle size determination. *J. Appl. Meteor.*, **9**, 86–103.
- , 1981: Techniques for probing cloud microstructure. *Clouds: Their Formation, Optical Properties, and Effects*, P. V. Hobbs and A. Deepak, Eds., Academic Press, 15–91.
- Korolev, A. V., and G. A. Isaac, 2005: Shattering during sampling by OAPs and HVPS. Part I: Snow particles. *J. Atmos. Oceanic Technol.*, **22**, 528–542.
- , J. W. Strapp, G. A. Isaac, and A. N. Nevzorov, 1998: The Nevzorov airborne hot-wire LWC-TWC probe: Principle of operation and performance characteristics. *J. Atmos. Oceanic Technol.*, **15**, 1495–1510.
- , G. A. Isaac, and J. Hallett, 1999: Ice particle habits in Arctic clouds. *Geophys. Res. Lett.*, **26**, 1299–1302.
- Lawson, R. P., B. A. Baker, C. G. Schmitt, and T. L. Jensen, 2001: An overview of microphysical properties of Arctic clouds observed in May and July during FIRE.ACE. *J. Geophys. Res.*, **106**, 14 989–15 014.
- , D. O'Connor, P. Zmarzly, K. Weaver, B. A. Baker, Q. Mo, and H. Jonsson, 2006a: The 2D-S (stereo) probe: Design and preliminary tests of a new airborne, high-speed, high-resolution particle imaging probe. *J. Atmos. Oceanic Technol.*, in press.
- , B. A. Baker, B. Pilson, and Q. Mo, 2006b: In situ observations of the microphysical properties of wave, cirrus, and anvil clouds. Part II: Cirrus clouds. *J. Atmos. Sci.*, in press.
- , —, P. Zmarzly, D. O'Connor, Q. Mo, J.-F. Gayet, and V. Shcherbakov, 2006c: Microphysical and optical properties of atmospheric ice crystals at South Pole Station. *J. Appl. Meteor. Climatol.*, in press.
- Locatelli, J. D., and P. V. Hobbs, 1974: Fall speeds and masses of solid precipitation particles. *J. Geophys. Res.*, **79**, 2185–2197.
- Mason, B. J., 1957: *Physics of Clouds*. Oxford University Press, 671 pp.
- Mitchell, D. L., R. Zhang, and R. L. Pitter, 1990: Mass-dimensional relationships for ice particles and the influence of riming on snowfall rates. *J. Appl. Meteor.*, **29**, 153–163.
- Ono, A., 1969: The shape and riming properties of ice crystals in natural clouds. *J. Atmos. Sci.*, **26**, 138–147.
- Strapp, J. W., F. Albers, A. Reuter, A. V. Korolev, U. Maixner, E. Rashke, and Z. Vukovic, 2001: Laboratory measurements of the response of a PMS OAP-2DC. *J. Atmos. Oceanic Technol.*, **18**, 1150–1170.
- Twohy, C. H., A. J. Schanot, and W. A. Cooper, 1997: Measurement of condensed water content in liquid and ice clouds using an airborne counterflow virtual impactor. *J. Atmos. Oceanic Technol.*, **14**, 197–202.
- Zuidema, P., B. Baker, Y. Han, J. Intrieri, J. Key, P. Lawson, S. Matrosov, M. Shupe, R. Stone, and T. Uttal, 2005: An Arctic springtime mixed-phase cloudy boundary layer observed during SHEBA. *J. Atmos. Sci.*, **62**, 160–176.